CERN - European Organization for Nuclear Research

LCD-Note-2011-028

Particle Flow Performance at CLIC

J. Marshall[*], A. Münnich [†], M. A. Thomson [*]

[*] *University of Cambridge, UK,* [†] *CERN, Switzerland*

January 16, 2012

Abstract

Particle Flow has been used very successfully in the studies for linear colliders. At CLIC with an energy of 3 TeV considerable machine background is present in the detector. Using timing cuts based on particle flow objects this background can be reduced significantly. A systematic study is carried out to understand the dependence of the jet energy resolution on the jet energy and angle. The performance of particle flow is evaluated based on the energy and mass resolution of *W* and *Z* particles in full simulation and reconstruction in the presence of background for both detector concepts considered for CLIC.

Contents

1 The Particle Flow Concept

Measurements of jet fragmentation at LEP provided detailed information about the composition of jets[1, 2]. In a typical jet, approximately 62% of the energy is carried by charged particles (mainly hadrons), whilst 27% is carried by photons, 10% by long-lived neutral hadrons and 1.5% by neutrinos. With a conventional approach to calorimetry, the energy of a jet would be reconstructed purely from the energy deposited in the electromagnetic and hadronic calorimeters (ECAL and HCAL respectively). In this way, 72% of the jet energy would be measured with a precision limited by the relatively poor HCAL resolution $\sigma(E)/E$ of typically $> 55\%/\sqrt{E\,(\mathrm{GeV})}$.

The particle flow approach to calorimetry and the jet energy measurement aims to reconstruct the four-vectors of all visible particles in an event. The reconstructed jet energy is then the sum of the energies of the individual particles in the jet. Charged particle momenta are measured in the tracking detectors and only energy measurements for photons and neutral hadrons are obtained from the calorimeters. In this way, the HCAL is used to measure only about 10% of the jet energy, resulting in significant improvements in jet energy measurements compared to conventional calorimetry.

Particle flow calorimetry requires fine granularity detectors and sophisticated software algorithms, so that the energy depositions from individual particles can be traced through the detector and cleanly distinguished from the depositions of other particles. Failure to accurately reconstruct the paths of individual particles can result in double counting of energy (e.g. failure to associate calorimeter hits with a reconstructed track) or loss of energy (e.g. incorrect merging of hits from a neutral hadron with those from a nearby charged hadron). It is this confusion, rather than the calorimetric performance that is the limiting factor for particle flow calorimetry.

PANDORAPFANEW [3] is an efficient and robust framework for developing and running algorithms for particle flow reconstruction. It currently offers more than 60 high performance and

well-documented algorithms for reconstruction and identification of individual particles in fine granularity detectors. The reconstruction performed by the default PANDORAPFANEW algorithms can be summarised as follows:

1. Tracks and calorimeter hits in an event are examined and self-describing objects are created for use in the reconstruction. Calibration factors are applied to hit energy depositions. Quality cuts are applied to identify tracks suitable for particle flow object (PFO) construction, rejecting tracks that are likely due to reconstruction failures.

2. Hits are clustered using a cone-based outward projective algorithm, working from innermost to outermost layer. Isolated hits in the calorimeters (defined on the basis of proximity to other hits) are neglected in this initial clustering.

3. The clustering algorithm is configured so that it tends to split up true clusters, rather than risk combining energy deposits from multiple particles. The resulting cluster fragments are then merged together by a series of algorithms following well-motivated topological rules. Isolated hits are added back into the collection at this stage.

4. Calorimeter clusters are associated to tracks, by comparing the properties of the clusters and the projected track states at the surface of the calorimeter.

5. If the energy of a calorimeter cluster does not match the associated track momentum, the cluster can be split-up, or merged with nearby fragments, by a number of statistical reclustering algorithms. The calorimeter hits in the relevant clusters can be reclustered using a series of differently configured clustering algorithms to try to improve the track-cluster compatibility.

6. Fragments of charged hadrons are identified and added to the correct calorimeter clusters, then the final PFOs are constructed. If a PFO contains tracks and associated clusters, the particle properties are extracted from the tracks. For neutral particles, calorimeter information is used. Particle identification functions are used to label particle types and to distinguish between photons and neutral hadrons.

The above processes are described in more detail in references [3, 4]. These documents demonstrate that particle flow calorimetry, and the PANDORAPFANEW algorithms, can in principle meet the challenging jet energy resolution goals for the linear colliders ILC and CLIC.

2 PFO Selector

The PANDORAPFANEW algorithms aim to reconstruct the four-vectors of all visible particles in an event. A jet-finding algorithm can then be used to identify individual jets, with the jet energy reconstructed as the sum of the energies of the PFOs in the jet. However, in the presence of beam-induced background, it is vital to identify and remove the background particles before the jet-finding stage. The approach used is to perform the particle flow reconstruction with full background, then apply timing cuts to the PFOs. This strategy exploits the fact that, for clusters

containing many hits, the mean cluster time can be identified rather accurately. With a single hit resolution in the order of ns, mean cluster times with an accuracy much better than 1 ns can be obtained.

To remove background particles at CLIC, a CLICPFOSELECTOR has been implemented in the MARLIN framework [8] and tested with overlaid $\gamma\gamma \to$ hadrons background. This processor calculates the time measurements for each PFO. For PFOs containing clusters, the measured time is calculated by first determining the median time of all hits in the cluster. The outlying 10% of hits in the cluster are then neglected and the remaining hits are used to calculate an energy-weighted mean value. If the PFO also contains a track, a helix fit to the track is used to calculate the arrival time of the track at the surface of the ECAL. This value is subtracted from the measured cluster time. If sufficient hits are available, timing information from the ECAL region may be used preferentially to that from the HCAL region. Timing information from the steel HCAL endcap may also be used in preference to information from the tungsten HCAL barrel.

Selection cuts to these measurements are applied to identify the PFO as signal or background. As the background particles are concentrated in the forward region, tighter timing cuts are applied to low p_T particles and to those flagged as being in the forward region. Different cuts are applied to charged particles with associated calorimeter clusters, charged particles without clusters, photons and neutral hadrons.

The optimal values for the cuts applied to the PFO timing measurements will likely depend on the requirements of the physics analysis using the reconstructed jets. For this reason, the CLICPFOSELECTOR has three recommended configurations, which allow it to apply 'default', 'loose' and 'tight' cuts to the reconstructed PFOs. The selection cuts used under these three configurations are fully described in Tables 1, 2 and 3.

To illustrate the power of suppressing machine background with the CLICPFOSELECTOR Figure 1 shows the reconstructed particle flow objects for a simulated $e^+e^- \to H^+H^- \to t\bar{b}b\bar{t}$ event at $\sqrt{s} = 3$ TeV. Assuming a time window of 10 ns for the silicon detectors, the ECAL and the HCAL endcap and 100 ns for the HCAL barrel, the background from $\gamma\gamma \to$ hadrons produces an average energy of approximately 1.2 TeV per event, mostly in the form of relatively low p_T particles at relatively low angles to the beam axis. As a result of the cluster-based tight timing cuts the average background level can be reduced to approximately 100 GeV with negligible impact on the underlying hard interaction.

3 Particle Flow Performance: A Technical Study

The goal is to study the dependence of the particle flow performance on the energy, the angle and the timing cuts needed for the physics analysis. For this purpose Z' at various masses ranging from 91 GeV to 3 TeV are generated. These decay at rest into light quarks producing two mono-energetic jets in the event. No jet reconstruction is carried out at this stage and backgrounds are not included. The full energy deposited in the detector E_{jj} is analysed to avoid a bias from jet reconstruction. The performance of fully reconstructed physics observables in the presence of background is presented in the following section. Both detector concepts under consideration for CLIC are studied: CLIC_SiD [9] and CLIC_ILD [10].

Table 1: Cuts applied by the CLICPFOSELECTOR in the 'default' configuration mode.

Region	p_T range	Time cut
Photons		
Central	$0.75\,\text{GeV} \leq p_T < 4.0\,\text{GeV}$	$t < 2.0\,\text{ns}$
$|\cos(\theta)| \leq 0.975$	$0\,\text{GeV} \leq p_T < 0.75\,\text{GeV}$	$t < 1.0\,\text{ns}$
Forward	$0.75\,\text{GeV} \leq p_T < 4.0\,\text{GeV}$	$t < 2.0\,\text{ns}$
$|\cos(\theta)| > 0.975$	$0\,\text{GeV} \leq p_T < 0.75\,\text{GeV}$	$t < 1.0\,\text{ns}$
Neutral hadrons		
Central	$0.75\,\text{GeV} \leq E_T < 8.0\,\text{GeV}$	$t < 2.5\,\text{ns}$
$|\cos(\theta)| \leq 0.975$	$0\,\text{GeV} \leq E_T < 0.75\,\text{GeV}$	$t < 1.5\,\text{ns}$
Forward	$0.75\,\text{GeV} \leq E_T < 8.0\,\text{GeV}$	$t < 2.0\,\text{ns}$
$|\cos(\theta)| > 0.975$	$0\,\text{GeV} \leq E_T < 0.75\,\text{GeV}$	$t < 1.0\,\text{ns}$
Charged particles		
All	$0.75\,\text{GeV} \leq p_T < 4.0\,\text{GeV}$	$t < 3.0\,\text{ns}$
	$0\,\text{GeV} \leq p_T < 0.75\,\text{GeV}$	$t < 1.5\,\text{ns}$

Table 2: Cuts applied by the CLICPFOSELECTOR in the 'loose' configuration mode.

Region	p_T range	Time cut
Photons		
Central	$0.75\,\text{GeV} \leq p_T < 4.0\,\text{GeV}$	$t < 2.0\,\text{ns}$
$|\cos(\theta)| \leq 0.975$	$0\,\text{GeV} \leq p_T < 0.75\,\text{GeV}$	$t < 2.0\,\text{ns}$
Forward	$0.75\,\text{GeV} \leq p_T < 4.0\,\text{GeV}$	$t < 2.0\,\text{ns}$
$|\cos(\theta)| > 0.975$	$0\,\text{GeV} \leq p_T < 0.75\,\text{GeV}$	$t < 1.0\,\text{ns}$
Neutral hadrons		
Central	$0.75\,\text{GeV} \leq E_T < 8.0\,\text{GeV}$	$t < 2.5\,\text{ns}$
$|\cos(\theta)| \leq 0.975$	$0\,\text{GeV} \leq E_T < 0.75\,\text{GeV}$	$t < 1.5\,\text{ns}$
Forward	$0.75\,\text{GeV} \leq E_T < 8.0\,\text{GeV}$	$t < 2.5\,\text{ns}$
$|\cos(\theta)| > 0.975$	$0\,\text{GeV} \leq E_T < 0.75\,\text{GeV}$	$t < 1.5\,\text{ns}$
Charged particles		
All	$0.75\,\text{GeV} \leq p_T < 4.0\,\text{GeV}$	$t < 3.0\,\text{ns}$
	$0\,\text{GeV} \leq p_T < 0.75\,\text{GeV}$	$t < 1.5\,\text{ns}$

Table 3: Cuts applied by the CLICPFOSELECTOR in the 'tight' configuration mode.

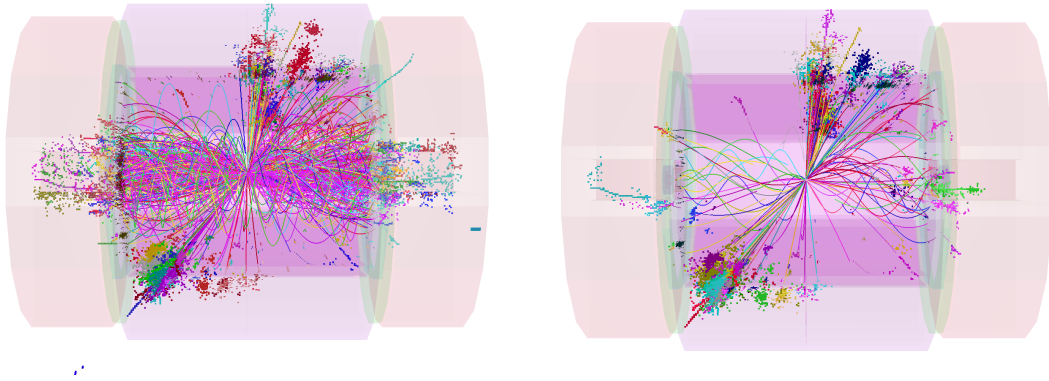| Region	p_T range	Time cut
Photons		
Central	$1.0\,\text{GeV} \leq p_T < 4.0\,\text{GeV}$	$t < 2.0\,\text{ns}$
$|\cos(\theta)| \leq 0.95$	$0.2\,\text{GeV} \leq p_T < 1.0\,\text{GeV}$	$t < 1.0\,\text{ns}$
Forward	$1.0\,\text{GeV} \leq p_T < 4.0\,\text{GeV}$	$t < 2.0\,\text{ns}$
$|\cos(\theta)| > 0.95$	$0.2\,\text{GeV} \leq p_T < 1.0\,\text{GeV}$	$t < 1.0\,\text{ns}$
Neutral hadrons		
Central	$1.0\,\text{GeV} \leq E_T < 8.0\,\text{GeV}$	$t < 2.5\,\text{ns}$
$|\cos(\theta)| \leq 0.95$	$0.5\,\text{GeV} \leq E_T < 1.0\,\text{GeV}$	$t < 1.5\,\text{ns}$
Forward	$1.0\,\text{GeV} \leq E_T < 8.0\,\text{GeV}$	$t < 1.5\,\text{ns}$
$|\cos(\theta)| > 0.95$	$0.5\,\text{GeV} \leq E_T < 1.0\,\text{GeV}$	$t < 1.0\,\text{ns}$
Charged particles		
All	$1.0\,\text{GeV} \leq p_T < 4.0\,\text{GeV}$	$t < 2.0\,\text{ns}$
	$0\,\text{GeV} \leq p_T < 1.0\,\text{GeV}$	$t < 1.0\,\text{ns}$

Figure 1: Reconstructed particles for a time window of 10 ns (100 ns in HCAL barrel) in a simulated $e^+e^- \rightarrow H^+H^- \rightarrow t\bar{b}b\bar{t}$ event in the CLIC_ILD detector with 60 BX of $\gamma\gamma \rightarrow$ hadron background overlaid (left). The effect of applying tight timing cuts on the reconstructed particles is shown on the right where the energy deposited in the detector by the background is reduced from 1.2 TeV to the level of 100 GeV.

The performance evaluation of the particle flow reconstruction is based on the resolution of

the jet energy E_j which is defined as:

$$\frac{\text{RMS}_{90}(E_j)}{\text{mean}_{90}(E_j)} = \frac{\text{RMS}_{90}(E_{jj})}{\text{mean}_{90}(E_{jj})}\sqrt{2} \tag{1}$$

The $\text{RMS}_{90}(E_{jj})$ and the $\text{mean}_{90}(E_{jj})$ are calculated from the total reconstructed energy distribution. The RMS_{90} is defined as the RMS in the smallest region of reconstructed energy that contains 90% of the events. It is introduced to reduce sensitivity to tails in a well defined manner as the energy distribution of particle flow objects is inherently non-Gaussian due to effects from confusion [4].

In this study the barrel region is defined as $|\cos(\theta)| < 0.7 (= 45.6°)$ and the endcap region between $0.7 < |\cos(\theta)| < 0.975 (= 12.8°)$ where the angle is calculated based on the quark content in the event.

3.1 Energy Resolution versus Jet Energy

With increasing energy the jets get narrower and distinguishing each individual particle becomes more difficult. In this case particle flow turns into energy flow and the confusion term dominates the energy resolution. At this point both detectors show similar performance. At lower energies CLIC_ILD benefits from its larger radius which is more beneficial for particle flow [4] and the degradation in energy resolution for low jet energies is not as pronounced as for CLIC_SiD. Figure 2 shows the jet energy resolution in dependence of the jet energy in the barrel region for both detector concepts.
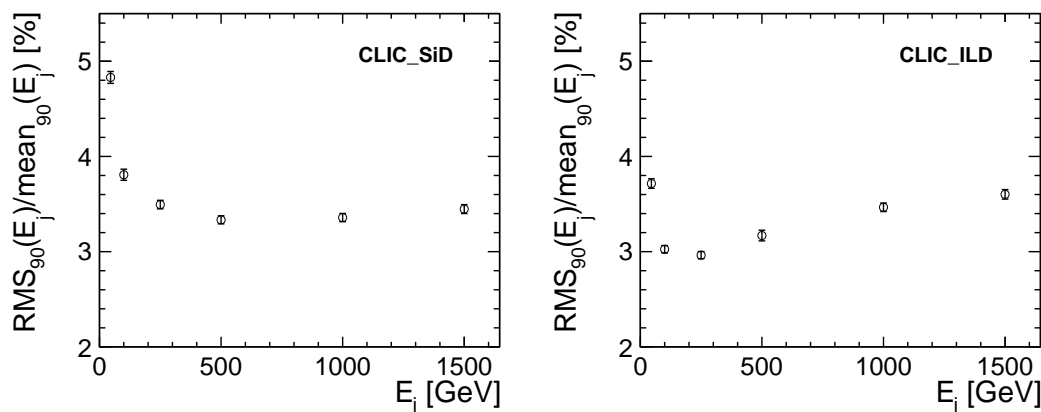

Figure 2: Jet energy resolution as function of the jet energy for CLIC_SiD (left) and CLIC_ILD (right) in the barrel region for Z' with different masses decaying at rest into two jets.

3.2 Energy Resolution versus Angle

Maintaining a good energy resolution throughout the full detector is challenging. Transition regions and possible gaps for cables or services complicate the association of single particles in a jet with their energy content. In the forward region jets are boosted and particles therefore closer together and the limited detector acceptance can lead to leakage, both affecting the energy resolution. To study these features events are grouped based on the quark angle and the performance of particle flow is evaluated within several angular regions. In the barrel region both detectors show only small variation with the angle of the quark jet as shown in Figure 3 for three different jet energies. The performance for CLIC_SiD is worse in the forward region, especially in the last bin due to angular coverage. The last bin covers the region $0.95 < |\cos\theta| < 0.975$ which means it goes to angles as small as $12.8°$. Table 4 shows that the angular acceptance is smaller for CLIC_SiD especially for the HCAL which covers only down to $15.5°$ and therefore misses more energy in the forward region. In the case of CLIC_ILD a dip in energy resolution occurs in the overlap between barrel and forward region around $|\cos\theta| = 0.75$. This is due to a gap between the ECAL barrel and ECAL endcap which is bigger in the CLIC_ILD detector as can be seen in Figure 4. The effect of this gap on the resolution is more pronounced for high energies.
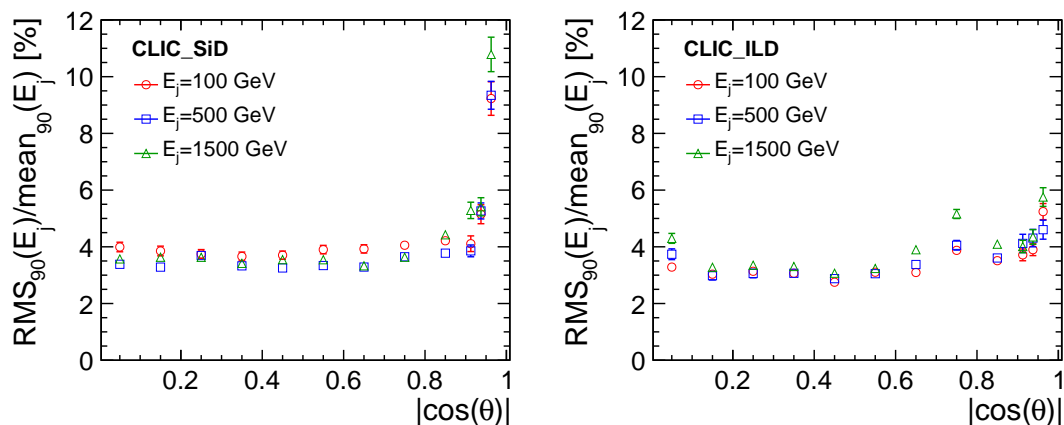

Figure 3: Jet energy resolution as a function of the event angle for CLIC_SiD (left) and CLIC_ILD (right) for Z' with different masses decaying at rest into two jets.

3.3 Timing Cuts

Without actually overlaying any background the impact of the timing cuts applied in the CLIC-PFOSELECTOR on the physics event is studied. Figure 5 shows the energy remaining in the event before applying the timing cuts and for each of the selections provided by the CLICPFO-SELECTOR specified in Tables 1, 2 and 3. The more stringent the cuts the more energy is cut away from the event. The changes get less significant with increasing energy which is illustrated in the comparison between Figure 5 at 91 GeV and Figure 6 at 1 TeV.

8

Table 4: Acceptance of calorimeter endcaps for CLIC_SiD and CLIC_ILD.

		R_i [mm]	Z [mm]	θ [°]
CLIC_SiD	ECAL	210	1657	7.2
	HCAL	500	1805	15.5
CLIC_ILD	ECAL	242	2450	5.6
	HCAL	400	2650	8.6
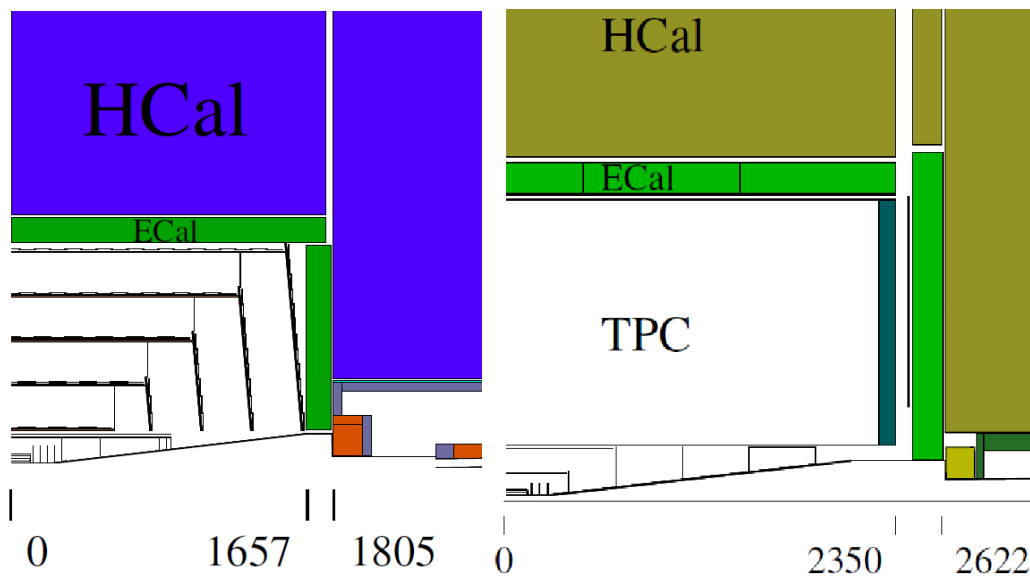
Figure 4: Detector geometry for CLIC_SiD (left) and CLIC_ILD (right). CLIC_ILD allows more space for cables between the barrel and the forward region whereas CLIC_SiD has an overlap of ECAL barrel and endcap in *r* direction.

At low jet energies the effect of the CLICPFOSELECTOR on the energy resolution is significant, but with increasing jet energy the performance is the same as with no cuts applied. The results are shown in Figure 7. Already without any timing cuts the total energy reconstructed in the event shows a slight shift towards lower values which is more pronounced in CLIC_SiD than CLIC_ILD. This effect is due to the calibration factors assigned in the software to the different contributions in the calorimeters sampling fractions. The calibration is based on the response of single particles and optimised for linearity for both CLIC_SiD and CLIC_ILD. For single particles the energy response in the calorimeters has a slope of 1. In dense jets however, the jet energy scale in CLIC_SiD deviates from 1 to lower values.
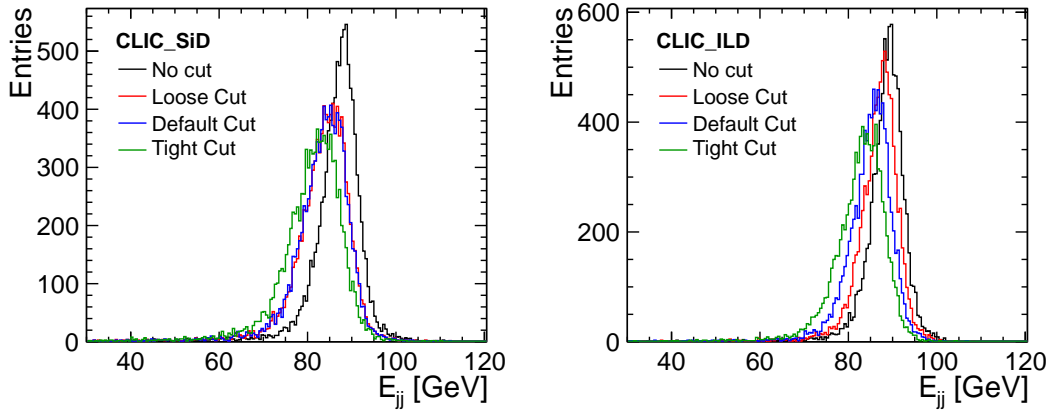
Figure 5: Effect of timing cuts on reconstructed energy at $\sqrt{s}$=91 GeV for CLIC_SiD (left) and CLIC_ILD (right).
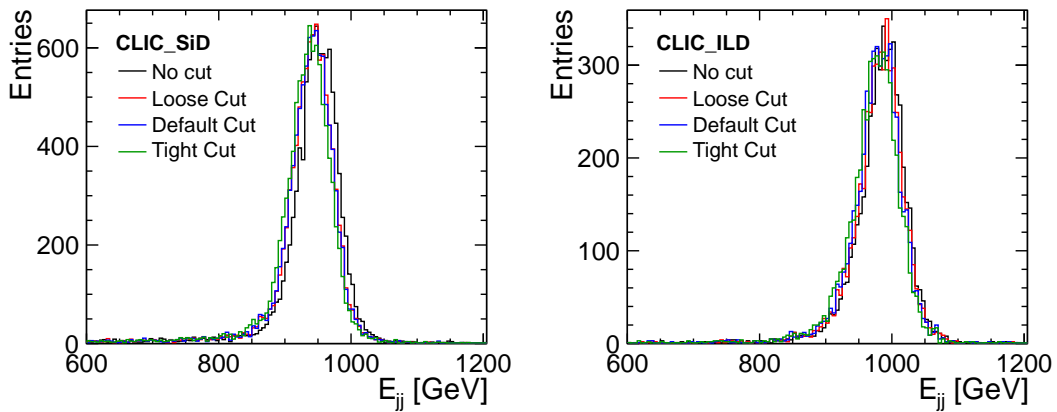

Figure 6: Effect of timing cuts on reconstructed energy at $\sqrt{s}$=1 TeV for CLIC_SiD (left) and CLIC_ILD (right).

4 Particle Flow: Physics Performance

4.1 $WW \rightarrow \mu\nu qq$

The first event sample to study the physics performance of particle flow contains two Ws, one decaying into a muon the other into quarks. Four different energies sets for each W were generated: 125, 250, 500 and 1000 GeV. The main background for physics at CLIC is the $\gamma\gamma \rightarrow$ hadron background. For each bunch crossing (BX), the number of $\gamma\gamma \rightarrow$ hadron background events to
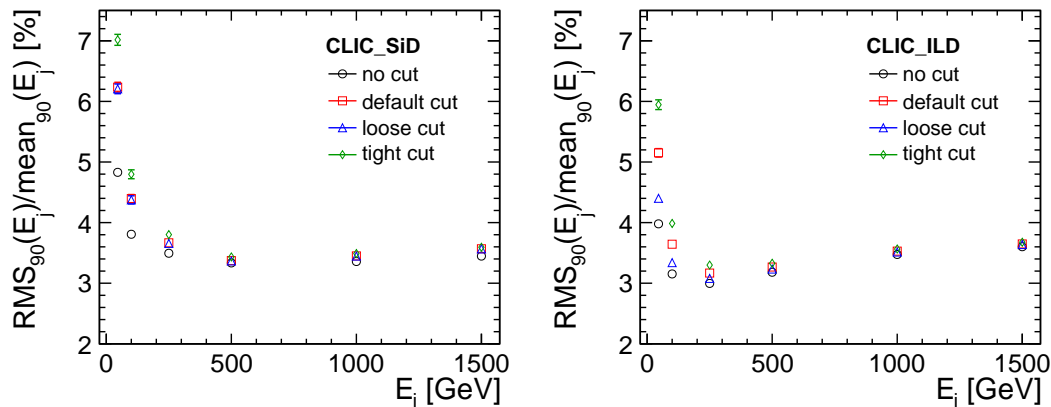
Figure 7: Effect of timing cuts on reconstructed energy versus energy for CLIC_SiD (left) and CLIC_ILD (right) for Z' with different masses decaying at rest into two jets.

be superimposed was drawn from a Poisson distribution assuming a mean of 3.2 events per BX [5, 6]. Each energy set is available with $\gamma\gamma \to$ hadron background overlaid (60 BX) and without (00 BX). In order to study the effect of the amount of $\gamma\gamma \to$ hadron background on the resolution a safety factor 2 was applied and 60 BX with 6.4 events of $\gamma\gamma \to$ hadron background per bunch crossing were fully simulated and reconstructed as well (2×60 BX).

The reconstruction and event selection was done in several steps:

- Lepton Removal:
  The muon and every particle around it within a cone of $|\cos\alpha| > 0.9$ is removed, leaving only the hadronic decay of one W in the event.

- Removal of Neutral Fragments:
  In the case of background this additional step is applied to remove low energetic neutral remnants in the forward region ($|\cos\theta| > 0.9$). These neutral clusters have a high probability to be fake neutral energy deposits due to a failed matching between the low p_T curling track with the calorimeter cluster. The minimal energy required for a neutral particle to remain in the event ranges from 1 to 8 GeV depending on $\sqrt{s}$ of the event. A systematic variation of this cut was carried out and it was found that the energy resolution benefits from introducing a threshold but once it is applied the actual value does not affect the energy resolution any more and it shows a flat response to increasing the minimal value further.

- Jet Reconstruction:
  After some evaluation of jet algorithms the FastJet library [7] was used. The kt algorithm is used in exclusive mode forcing the event into two jets. A scan of the R parameter for the jet cone size was carried out for every combination of energy, with and without background, and for all collections of the CLICPFOSELECTOR (default, loose and tight).

11

There is no significant difference for the three different timing selections. With background the best *R* value was found to be 0.7 and without background an *R* value of 1.5 is used. Figure 8 shows an example of the *R* parameter scan for CLIC_SiD at a *W* energy of 500 GeV with 60 BX of background.
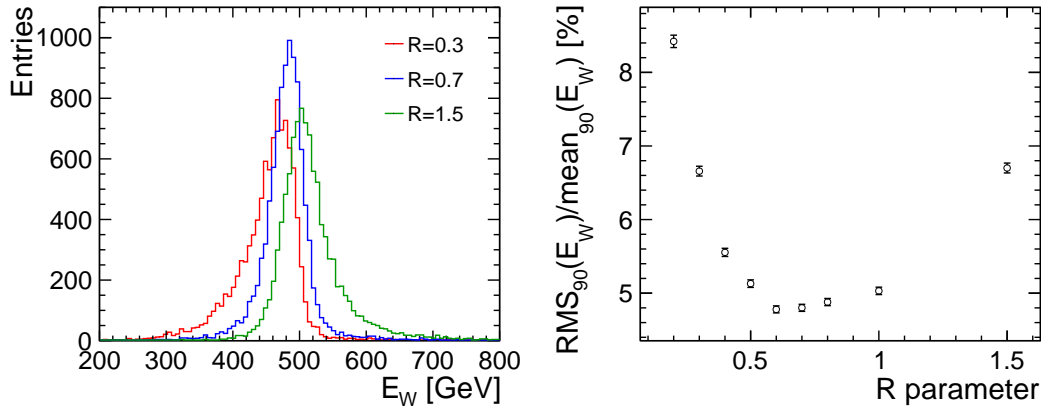

Figure 8: Jet reconstruction: Scan of the *R* parameter for CLIC_SiD at a *W* energy of 500 GeV with 60 BX of background. The reconstructed *W* energy is shown on the left for three different *R* values and on the right the energy resolution in dependence on the *R* parameter is shown.

The performance of particle flow is closely linked to the quality of the jet reconstruction. Using one jet algorithm over a wide range of jet energies does not always give the best performance. For low energies for example the ee_kt algorithm does yield a better mass resolution than the kt algorithm in the case of no background and vice versa for high energies. But with $\gamma\gamma \rightarrow$ hadron background the ee_kt algorithm cannot be used as it picks up all the background particles. For this reason and for a cleaner comparison of events with and without background the same jet reconstruction was used for all energies and all data sets.

- Event Selection:
  Both jets are required to have $|\cos\theta| < 0.9$ to stay well within the detector acceptance. In addition a lower limit on the angle between the two jets is applied to reject events were the jet reconstruction failed. The limit depends on the energy of the *W* and is based on the expected range of angles calculated from kinematics.

Figures 9 and 10 demonstrate the need for the timing cuts in the presence of background. The energy and mass distribution of the reconstructed *W* at 500 GeV are shown if no timing cuts are applied and for the tight selection. For comparison the corresponding distribution in the case of no background is displayed as well. Without applying any timing cuts, too many background particles remain in the event and are reconstructed as part of the jet, shifting the energy distribu-

tion to higher values. The mass distribution is more sensitive to additional background particles attributed to the reconstructed jet because these affect not only the jet energy but also the jet axis.
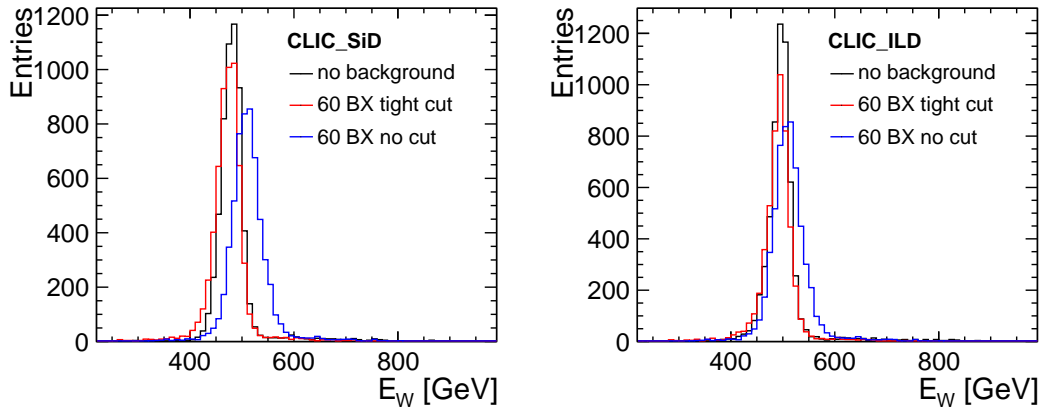

Figure 9: Energy distribution of the reconstructed *W* at an energy of 500 GeV with 60 BX of background if no timing cuts are applied and for the tight selection for CLIC_SiD (left) and CLIC_ILD (right). For reference the distribution is also shown if no background is present.
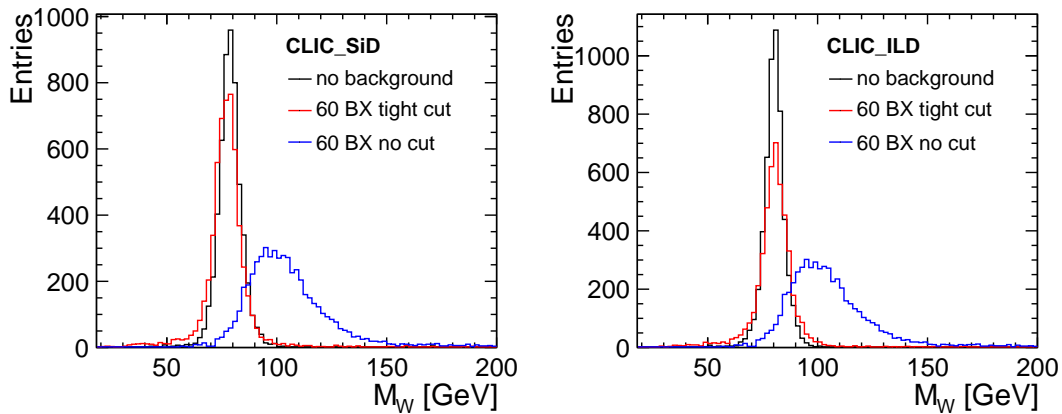

Figure 10: Mass distribution of the reconstructed *W* at an energy of 500 GeV with 60 BX of background if no timing cuts are applied and for the tight selection for CLIC_SiD (left) and CLIC_ILD (right). For reference the distribution is also shown if no background is present.

In the following only the tight collection will be studied as the difference between the three timing cut selections is minimal. As for the technical study presented in the previous section the RMS_{90} and $mean_{90}$ from the distribution of the jet energy and the jet mass are calculated. With the overlay of 60 BX of background the energy and mass distribution get distorted and tails become more prominent. The RMS_{90} method to calculate the resolution is robust against these changes in shape and increasing tails, but it includes all the features of the distribution and not just the main part of the peak. Therefore the resolutions given are purely a measure of the peak quality but cannot be directly used to extrapolate to a separation power between Ws and Zs. This will be addressed in section 4.3.

Figure 11 shows the energy resolution of the reconstructed W in dependence of the W energy without background and for the nominal as well as for twice the nominal amount of background. Figure 12 shows the corresponding mass resolution of the reconstructed W.
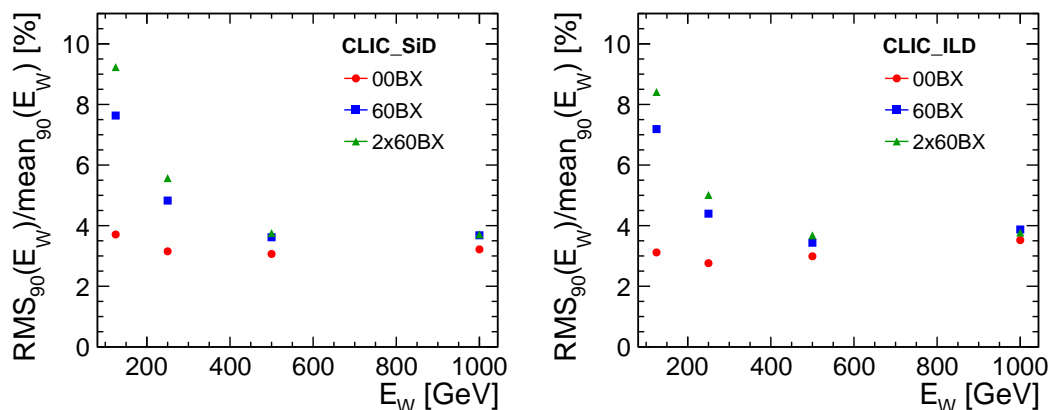

Figure 11: Energy resolution of the reconstructed W for CLIC_SiD (left) and CLIC_ILD (right), each with 60 BX, 2×60 BX of $\gamma\gamma \to$ hadron background and without background.

Without background the results are comparable to the resolutions obtained in the technical study without jet reconstruction. In the presence of background the degradation of the energy resolution at lower energies is significant. With increasing W energy the effect of background becomes less dominant for the energy resolution. As the mass resolution is more sensitive to the jet quality and reconstructed direction of the jets a larger degradation remains as well for higher W energies. With 60 BX of background both CLIC_SiD and CLIC_ILD show almost the same performance in energy and mass resolution. The effect of a factor two more background is again more visible at lower energies but the decrease in resolution is not too large.

4.2　$ZZ \to \nu\nu qq$

In order to study the separation of W and Z the event sample $e^+e^- \to ZZ \to \nu\nu qq$ was chosen to obtain the performance of particle flow for Z particles. Z bosons of different energies are
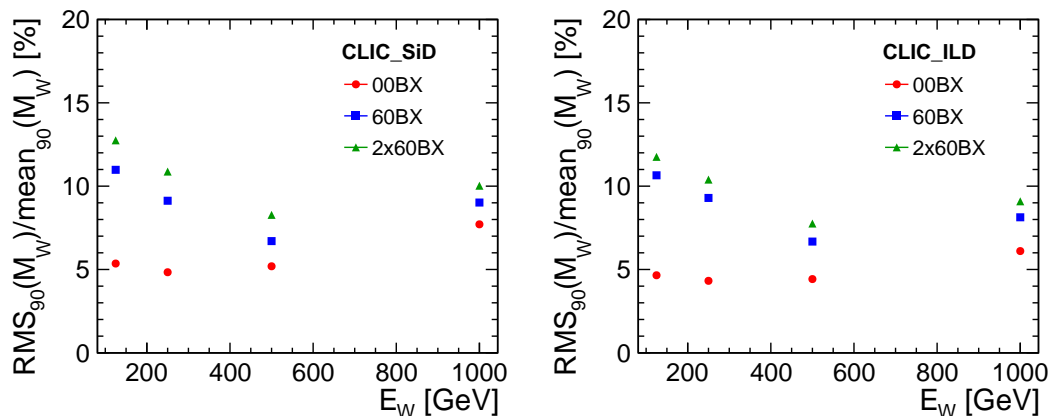
Figure 12: Mass resolution of the reconstructed W for CLIC_SiD (left) and CLIC_ILD (right) each with 60 BX, 2×60 BX of $\gamma\gamma \to$ hadron background and without background.

studied: 125, 250, 500 and 1000 GeV. Events were fully simulated and reconstructed without and with 60 BX of $\gamma\gamma \to$ hadron background and as well, like for the WW data sets, with a factor two more of $\gamma\gamma \to$ hadron background (2×60 BX). The same reconstruction and event selection procedure as for the Ws in the previous section is used.

Figure 13 shows the energy and Figure 14 the mass resolution for both detector concepts. The results are very similar to the performance obtained for the Ws.
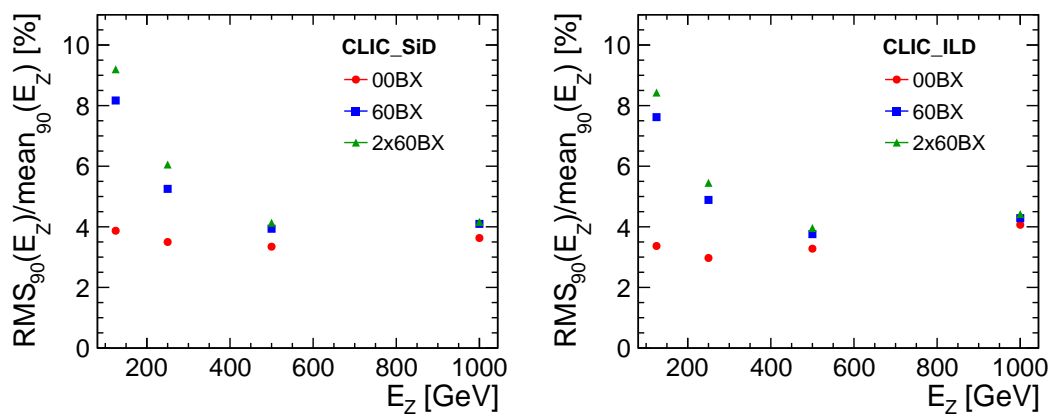
Figure 13: Energy resolution of the reconstructed Z for CLIC_SiD (left) and CLIC_ILD (right) each with and without background.
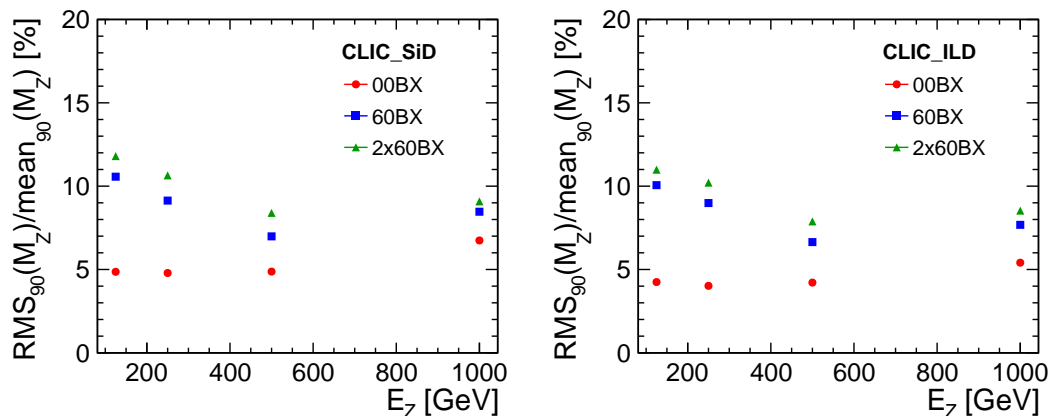
Figure 14: Mass resolution of the reconstructed Z for CLIC_SiD (left) and CLIC_ILD (right) each with and without background.

4.3 Separation Power: W and Z

One of the goals of a fine grained calorimeter and particle flow is to be able to distinguish between W and Z particles. Using the data sets described in section 4.1 and 4.2 the separation capability can be studied. Figures 15 and 16 show the reconstructed mass peak for W and Z and the corresponding envelope of the sum for W and Z both with an energy of 500 GeV in both detector concepts. Without background the two peaks remain clearly separated. In the case of 60 BX of $\gamma\gamma \rightarrow$ hadron background the W and Z peak start to overlap significantly.

The separation is calculated by applying an optimal cut in such a manner that the amount of mis-identified events is minimised. In the case of ideal Gaussian distributions a mis-identification of 15.8% corresponds to a separation of 2σ [4]. Figure 17 illustrates this methods for two ideal Gaussian distributions. If non-Gaussian tails are present in the distribution the separation drops below 2σ even if the main peaks are still 2σ apart. The obtainable separation is limited by the natural width of the W and Z to an identification efficiency of 94%.

Figure 18 shows the separation in dependence on the W or Z energy for both detector concepts. The shape is roughly anti-proportional to the mass resolution.

Table 5 summarises the obtained mass resolution for W and Z, the separation power and the identification efficiency for the different energies for CLIC_SiD and Table 6 for CLIC_ILD.

In physics analyses like the measurement of chargino and neutralino pair production both W and Z are present as decay products of these SUSY particles. Figure 19 visualises the separation between W and Z in full hadronic WW and ZZ final states from chargino and neutralino decays.
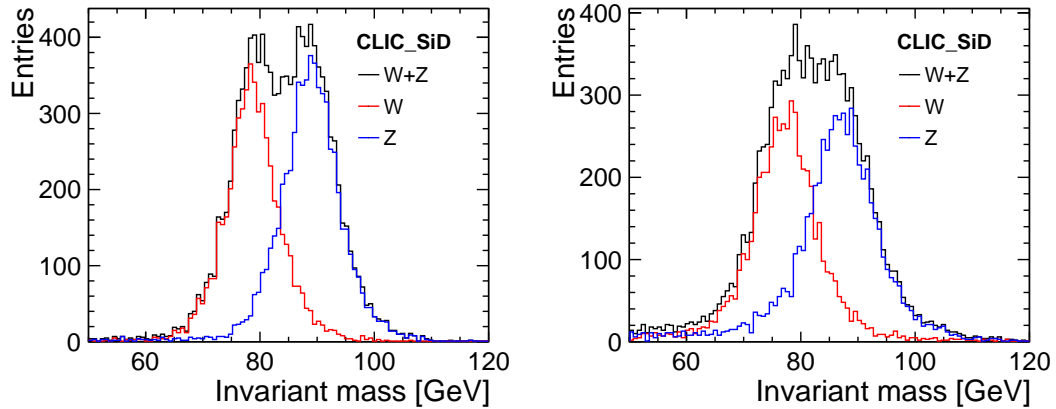
Figure 15: Mass distribution of the reconstructed *W* and *Z* for CLIC_SiD with $E_{W,Z} = 500$ GeV without background (left) and with 60 BX of background (right). Without background the separation is 1.9 σ and with 60 BX of background the separation drops to 1.7 σ.
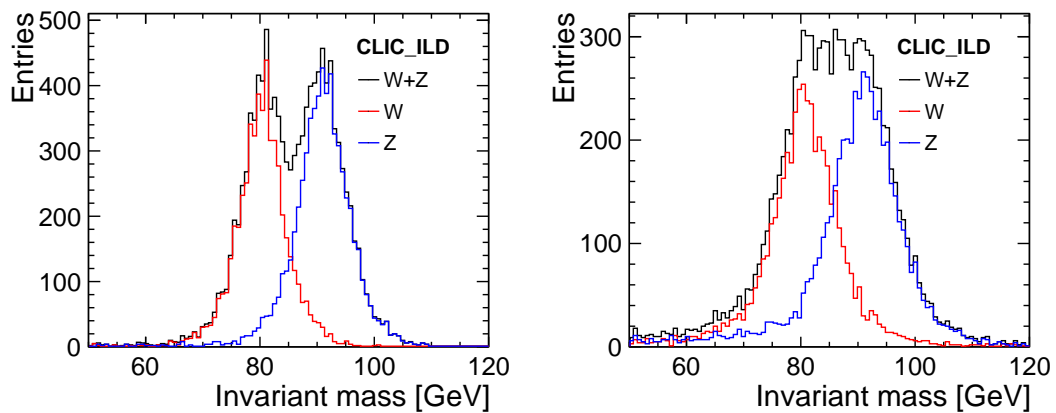

Figure 16: Mass distribution of the reconstructed *W* and *Z* for CLIC_ILD with $E_{W,Z} = 500$ GeV without background (left) and with 60 BX of background (right). Without background the separation is 2.0 σ and with 60 BX of background the separation drops to 1.6 σ.
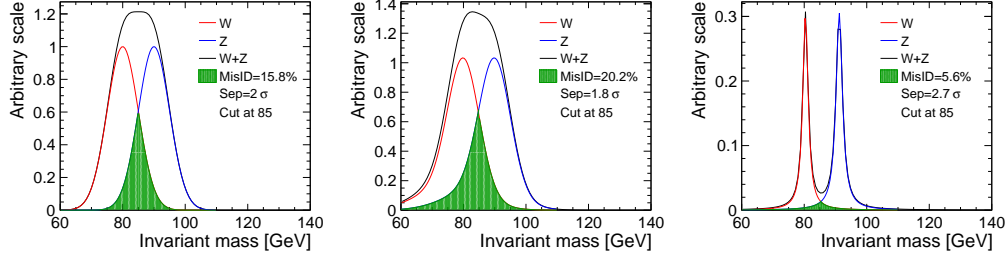
Figure 17: Illustration of separation extraction method: The left picture shows the basis of the definition used for the separation: Two perfect Gaussians each with a width σ that are 2 σ apart create an overlap region of 15.8% of mis-identified events for an optimal cut that is located at the intersection point of both distributions. In the middle the influence of tails is illustrated: Even though the main peaks still are 2 σ apart the separation power is degraded by the contribution of the tail. On the right the best achievable case is illustrated where the width of the peaks are only limited by the natural width of the W and Z following a Breit-Wigner distribution.
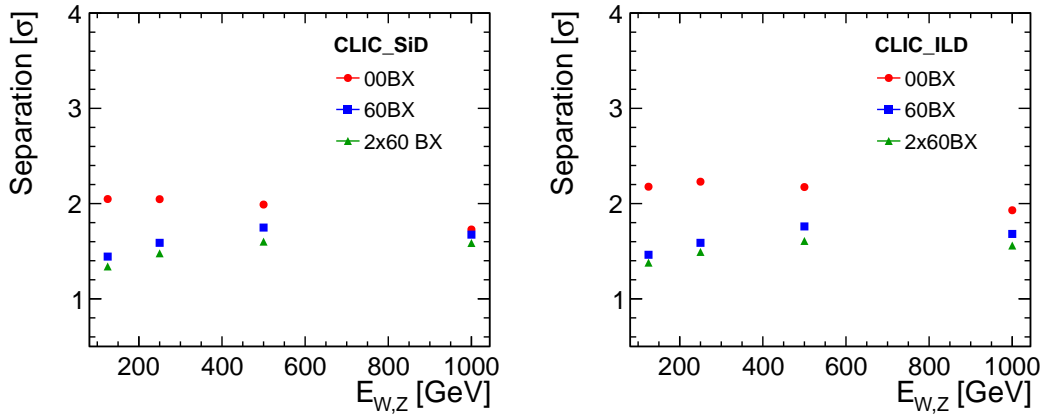

Figure 18: Separation between W and Z peak with no background and with 60 BX of background for CLIC_SiD (left) and CLIC_ILD (right).

4.4 Measurement of Missing Momentum

Resolution of Missing Momentum

For this study the event samples $ZZ \rightarrow \nu\nu qq$ from section 4.2 are reused. The jet reconstruction remains the same and the only event selection is that both jets fulfil the requirement $|\cos\theta| < 0.9$. The four different energy points $\sqrt{s}=$250, 500, 1000 and 2000 GeV are combined into one

Table 5: Separation between W and Z and corresponding mass resolution for CLIC_SiD.

BX	$E_{W,Z}$ [GeV]	$\sigma_{m(W)}/m(W)$ [%]	$\sigma_{m(Z)}/m(Z)$ [%]	Separation [σ]	ε [%]
00 BX	125	5.3	4.9	2.0	85
	250	4.8	4.8	2.0	85
	500	5.2	4.9	2.0	84
	1000	7.7	6.7	1.7	78
60 BX	125	11.0	10.6	1.4	69
	250	9.1	9.1	1.6	74
	500	6.7	7.0	1.7	78
	1000	9.0	8.5	1.7	76
2×60 BX	125	12.7	11.8	1.3	66
	250	10.9	10.6	1.5	70
	500	8.3	8.4	1.6	74
	1000	10.0	9.1	1.6	74

Table 6: Separation between W and Z and corresponding mass resolution for CLIC_ILD.

BX	$E_{W,Z}$ [GeV]	$\sigma_{m(W)}/m(W)$ [%]	$\sigma_{m(Z)}/m(Z)$ [%]	Separation [σ]	ε [%]
00 BX	125	4.6	4.2	2.2	88
	250	4.3	4.0	2.2	89
	500	4.4	4.2	2.2	88
	1000	6.1	5.4	1.9	87
60 BX	125	10.7	10.1	1.5	70
	250	9.3	9.0	1.6	74
	500	6.7	6.6	1.8	79
	1000	8.1	7.7	1.7	77
2×60 BX	125	11.8	11.0	1.4	67
	250	10.4	10.2	1.5	71
	500	7.8	7.9	1.6	74
	1000	9.1	8.5	1.6	73

data set as the interesting quantity for this study is the transverse momentum and not the full energy. The measured quantity is the missing transverse momentum $p_{\text{T,miss}}$. In order to obtain the resolution of $p_{\text{T,miss}}$ the vector sum of all particles reconstructed in the two jets is computed. From the Monte Carlo truth the missing transverse momentum of the neutrinos $p_{\text{T,miss,true}}$ is calculated. The width of the distribution when subtracting the true value $p_{\text{T,miss,true}}$ from the reconstructed $p_{\text{T,miss}}$ gives the precision of the missing momentum measurement. The left plot of Figure 20 shows the distribution of the difference between the measured and the true missing
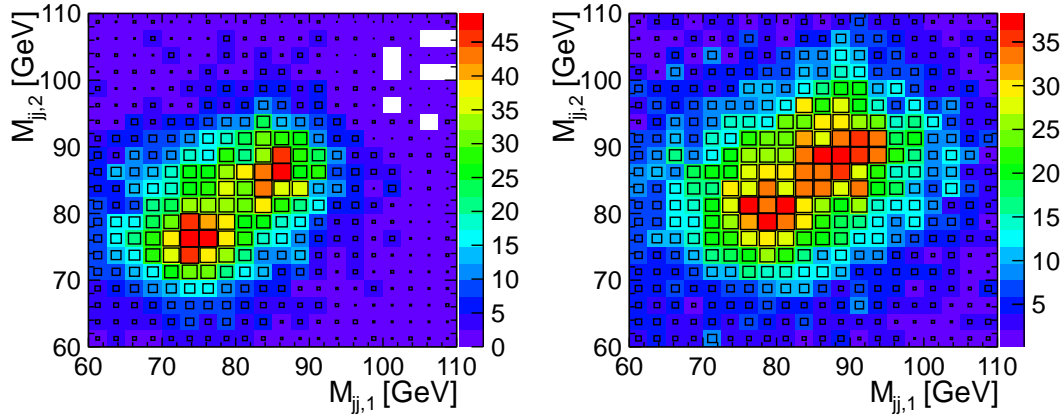
Figure 19: Separation of *W* and *Z* from the chargino decay without overlay (left) and with 60 BX of background (right) for CLIC_SiD.

transverse momentum for all values of p_T in the data sample. On the right the resolution of the missing transverse momentum as function of p_T is displayed. The binning in p_T is chosen in a way that each bin has 2000 entries. This can cause a slight difference in the binning between the cases with and without background. For each bin in p_T the RMS_{90} of the $\Delta p_{T,miss}$ distribution is calculated. The missing momentum can be measured with the same precision as the jet energy resolution.
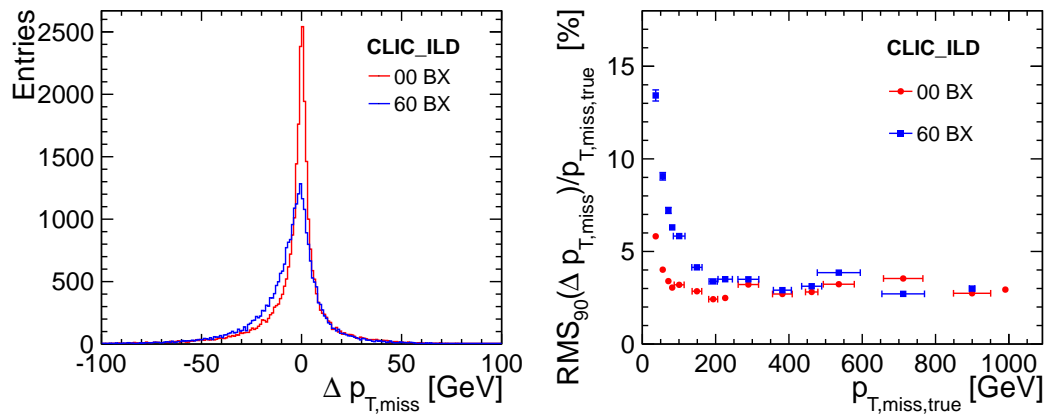

Figure 20: Distribution to determine the resolution of missing transverse momentum (left) and the resolution itself (right) without background and with 60 BX of background for CLIC_ILD based on $ZZ \rightarrow \nu\nu qq$ events.

Fake Missing Momentum

Many physics analyses rely on the measurement of missing momentum, especially in SUSY scenarios. Detector coverage plays a crucial role, but also the reconstruction can affect the measured missing momentum. Particles that are lost or falsely reconstructed create false missing momentum in the event. In this section the order of magnitude of this fake missing momentum caused by the reconstruction using particle flow is addressed. based on events without missing energy like the previously used Z' particles decaying at rest into light quarks. The events are reconstructed into 3 jets to account for the two quark jets and the colour reconnection between them. If only 2 jets are allowed the jet algorithm does not pick up all the energy in the event. As a cross check also 4 jets and n jets were reconstructed and both yield the same result as reconstructing the event into 3 jets. No event quality requirements are enforced. The momentum in x and y of all particles in jets is calculated. As there is no true missing momentum the distributions in x and y are the same and x is chosen for the study. Figure 21 shows the distribution of missing momentum in x on the left for a Z' of 91 GeV with and without background for CLIC_ILD. For each energy the RMS_{90} of this distribution is calculated and shown in Figure 21 on the right. The amount of fake missing momentum rises linear with the full energy deposited in the detector. Overall the level of fake missing momentum is at the level of 1-2% of the event energy.
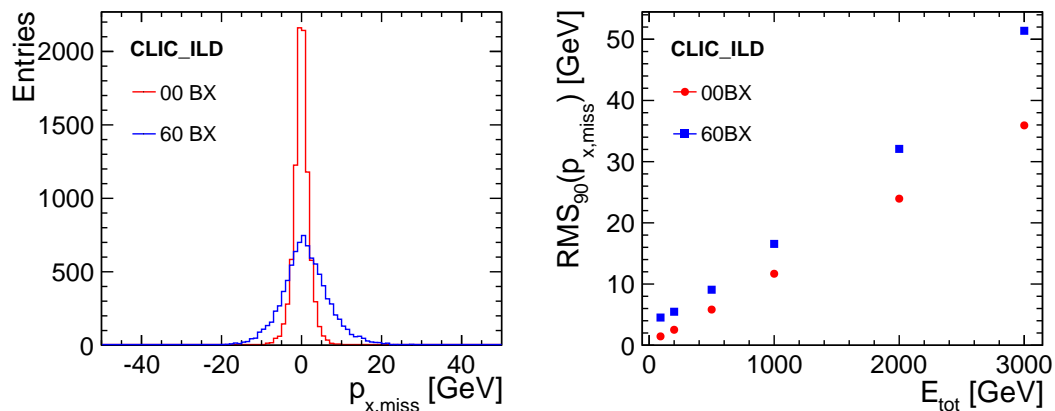

Figure 21: Distribution of fake missing momentum in x (left) for E_{tot}=91 GeV and the RMS_{90} of these distributions (right) both with no background and with 60 BX of background for CLIC_ILD based on Z' with different masses decaying at rest into two jets.

5 Summary and Outlook

The Particle Flow Algorithm is a powerful tool to achieve very good energy and mass resolutions. Even in the challenging environment of CLIC with beam induced-backgrounds timing

cuts on the particle level after full reconstruction with particle flow can significantly reduce the contribution of background particles.

The systematic effects of detector acceptance and energy dependence of particle performance were addressed and understood with a technical study of mono-energetic jets with energies up to 1.5 TeV.

Two physics channels providing *W* and *Z* particles were chosen to study the performance with jet reconstruction and in the presence of background. The energy and mass resolutions achieved are very promising. At higher energies the affect of the $\gamma\gamma \to$ hadron background on the energy resolution is negligible. The mass resolution is more sensitive and is closely related to the quality of reconstructed jets and their direction. A single jet finding algorithm cannot cover the full range of energies studied here. The interplay between different jet algorithm and the dependence on energy and event topology still needs to be investigated systematically. Nevertheless, *W* and *Z* separation remains possible with the added background but it becomes more challenging. In the presence of background both detector concepts CLIC_SiD and CLIC_ILD show very similar performance.

The precision of measuring missing momentum is at the same level as the jet energy resolution. The level of fake missing momentum is at the level of 1-2% of the event energy.

References

[1] I.G. Knowles, G.D. Lafferty, *Hadronization in Z0 decay*, J. Phys. G 23 (1997) 731.

[2] M.G. Green, S.L. Lloyd, P.N. Ratoff, D.R. Ward, *Electron-Positron Physics at the Z*, IoP Publishing, 1998.

[3] J.S. Marshall, *Redesign of PandoraPFA*, Report at IWLC 2010, October 19, 2010, Geneva.

[4] M.A. Thomson, *Particle Flow Calorimetry and the PandoraPFA Algorithm*, Nucl.Instr. and Meth. A 611 (2009) 25.

[5] P. Schade, A. Lucaci-Timoce, *Description of the signal and background event mixing as implemented in the Marlin processor OverlayTiming* LCD-Note-2011-006

[6] C. Grefe; *OverlayDriver - an Event Mixing Tool for org.lcsim* LCD-Note-2011-032

[7] M. Cacciari, G.P. Salam, *Dispelling the N3 myth for the kt jet-finder* Phys. Lett.B 641 (2006) 57

[8] F. Gaede, *Marlin and LCCD: Software tools for the ILC*, Nucl.Instr. and Meth. A 559 (2006) 177.

[9] C. Grefe, A. Münnich , *The CLIC_SiD_CDR Detector Model for the CLIC CDR Monte Carlo Mass Production* , LCD-Note-2011-009, 2011

[10] A. Münnich, A. Sailer, *The CLIC ILD CDR Geometry for the CDR Monte Carlo Mass Production*, LCD-Note-2011-002, 2011